Retained strength of UHTCMCs after oxidation at 2278 K

Galizia, Pietro; Vinci, Antonio; Zoli, Luca; Monteverde, Frederic; Binner, Jon; Venkatachalam, Vinothini; Lagos, Miguel A.; Reimer, Thomas; Jain, Neraj; Sciti, Diletta

DOI:
10.1016/j.compositesa.2021.106523

Document Version
Peer reviewed version

Citation for published version (Harvard):
Galizia, P, Vinci, A, Zoli, L, Monteverde, F, Binner, J, Venkatachalam, V, Lagos, MA, Reimer, T, Jain, N & Sciti, D 2021, 'Retained strength of UHTCMCs after oxidation at 2278 K', *Composites Part A: Applied Science and Manufacturing*, vol. 149, 106523. https://doi.org/10.1016/j.compositesa.2021.106523

Retained strength of UHTCMCs after oxidation at 2278 K

Pietro Galizia[1], Antonio Vinci[1*], Luca Zoli[1], Frederic Monteverde[1], Jon Binner[2], Vinothini Venkatachalam[2], Miguel. A. Lagos[3], Thomas Reimer[4], Neraj Jain[4], Diletta Sciti[1]

* Corresponding author

[1] CNR-ISTEC, National Research Council of Italy, Institute of Science and Technology for Ceramics, Via Granarolo, Faenza (RA), 64-48018, Italy

[2] School of Metallurgy and Materials - University of Birmingham, Birmingham B15 2TT, UK

[3] TECNALIA, Basque Research and Technology Alliance (BRTA), Mikeletegi Pasealekua 2, 20009 Donostia-San Sebastián, Spain

[4] DLR German Aerospace Center, Institute of Structures and Design, Pfaffenwaldring 38-40, 70569 Stuttgart, Germany

Abstract

In the frame of Horizon 2020 European C^{3}HARME research project, the manufacture of ZrB_2-based CMCs was developed through different processes: slurry infiltration and sintering, radio frequency chemical vapour infiltration (RF-CVI) and reactive metal infiltration (RMI). To assess the high temperature stability, room temperature bending strength was measured after oxidizing the samples at 2278 K and compared to the strength of the as-produced materials. Microstructures were analysed before and after the thermal treatment to assess the damage induced by the high temperature oxidation. Short fibre-reinforced composites showed the highest retained strength (>80 %) and an unchanged stress-strain curve.

Keywords: A. Ceramic-matrix composites (CMCs); B. Cure behaviour; B. Environmental degradation; D. Mechanical testing

1 Introduction

A novel class of ultra-high temperature (UHT) ceramic-matrix composites (CMCs), progressively recognized as UHTCMCs, is currently under extensive study within the Horizon 2020 European C^3HARME research project [1,2]. The C^3HARME acronym stands for Next Generation Ceramic Composites for Harsh Combustion Environment and Space. In fact, the main application field of UHTCMCs developed in C^3HARME research project is aerospace, in particular new technological solutions for thermal protections during re-entry or hot components of combustion chambers for propulsion. Besides the well-known advantages coming from the adoption of the CMC concept like the reduced specific weight coupled with improved damage tolerance to strain failure, another added-value functionality was considered during the design of such class of out-performing UHTCMCs: the resistance to ultra-high temperature and oxidizing atmospheres [3–11]. This technological achievement could vastly improve the efficiency of the propulsion systems, and the durability of the thermal protection systems (TPSs) [12,13]. UHTCMCs can be produced in a variety of methods. The most-simple process consists in the use of chopped fibres, mixed with a UHTC matrix by conventional powder mixing methods, followed by sintering via hot pressing. The easiness of the process is counterbalanced by a lower damage tolerance with respect to the other UHTCMCs, due to the relatively low fibre length; hundreds of micrometers. For achieving higher damage tolerance, continuous fibres are envisaged. In the majority of cases, the first step for UHTCMC production is the infiltration of a fibre preform by a UHTC-based slurry. Then, the remaining porosity can be filled by polymer infiltration and pyrolysis, or by chemical vapour infiltration, or by reactive metal infiltration, or even by a combination of these methods. Alternatively, for slurry impregnated laminates (e.g. with planar geometry) sintering at high temperature can achieve the matrix densification. The resulting materials have rather different features, in terms of UHTC content, fibre content, fibre/matrix interface, matrix compactness, which is reflected in markedly diverse thermomechanical properties [5,14–17]. Preliminary studies

on mechanical properties of these composites showed promising strength up to 2373 K [18], although thermal damage can occur during heating [19–22]. However, to the best of our knowledge, no study has been carried out on oxidation resistance at temperature above 2273 K and its effect on mechanical properties.

For the first time, the present study has the purpose of assessing the intrinsic thermal stability of different UHTCMCs, including short fibre and continuous fibre UHTCMCs consolidated by sintering, CVI UHTCMCS and RMI UHTCMCs. To this aim, the flexural strength was measured by fracturing samples before and after oxidation treatment at above 2273 K, for two minutes, to determine the extent of strength deterioration amongst different subclasses of UHTCMCs.

2 Experimental

2.1 Materials

Materials for the present investigation were produced through different methods and divided in four main classes, depending on their composition or fabrication technology. The division into classes, detailed compositions and other information are reported in Table 1. Generally speaking, all compositions contained HC-Starck ZrB_2 GRADE B, whilst for the fibres different commercial products were used, as indicated case by case.

Two variants of short fibres composites were fabricated. *CFHP*: This composite was manufactured by mixing ZrB_2 powder with 40 vol.% chopped C_f (Nippon Graphite Fibre Corporation, XN60) and minor amounts (3%) of SiC through wet milling. The powder mixture was ball-milled for 24 hours in absolute ethyl alcohol using SiC media. The slurry was then dried in a rotary evaporator, sieved and hot pressed at 2173 K with an applied pressure of 40 MPa. *MFSPS*: A ZrB_2 + 10 vol.% SiC powder mixture was dry mixed with milled carbon fibres (Nippon Graphite Fibre Corporation, HC-600) to obtain a composite with a total fibre content of 40 vol.%. The powder mixture was consolidated by spark plasma sintering in vacuum (10^{-2} Pa) at 2173 K, 50 MPa, holding time 5 min. The two main differences between this material and CFHP is the use of milled fibres, e.g. with

length of 150 μm, the matrix composition (see Table 1) and the consolidation by spark plasma sintering (SPS) rather than HP.

Other two variants of continuous fibre composites, consolidated with hot pressing were produced as follows: *SIHP-1 and 2*: Powder mixtures consisting of ZrB_2 plus SiC were prepared by ball-milling in ethyl alcohol and drying by rotary evaporator. With these mixtures, aqueous slurries were prepared using poly-acrylates at different molecular weight as dispersant to tailor the fibre volumetric amount up to about 50 vol.%. The composites were fabricated by infiltrating unidirectional fabrics (Nippon Graphite Fibre Corporation, UF-XN80-300) stacked in a 0/0° arrangement. The nominal formulations (vol.%) are reported in Table 1. The green assemblies were sintered by hot-pressing (HP) at 2173 K, 40 MPa of linear applied pressure.

Two types of CVI composites were prepared, using 2.5D continuous C_f preforms (PANOX, 23 vol.% C_f, SurfaceTransforms plc., Cheshire, UK) with fabric layers stacked in an arrangement of random/0°/random/90°/random orientation fibres, where 0° and 90° are unidirectional layers, in plane and out of plane respectively and the random layers were formed as a result of Surface Transform's needling process. *CVI-1*: Ethanol based slurries containing ZrB_2 and polyethylene imine (PEI) dispersant were introduced into the 2.5 D preform by a manual injection process [23]. After injection, the preforms containing about 29% ZrB_2 were cleaned and dried in an air oven and further densified with pyrolytic carbon using a radio frequency (RF) heated chemical vapour infiltration process (RF-CVI), reaching the final nominal composition reported in Table 1. *CVI-2:* This composite is a variant of CVI-1, where the injected slurry had a different composition, namely 15 vol.% ZrB_2 + 10 vol.% SiC + 5 vol.% Y_2O_3, using SiC and Y_2O_3 nanopowders. The preform was again subsequently densified by the RF-CVI process, reaching the final nominal composition reported in Table 1.

Finally, the last 2 composites were obtained by the reactive metal infiltration process (RMI). *RMI-1 and 2*: Both samples were manufactured using UF-XN80-300 unidirectional laminates with uncoated fibres. The initial fibre volume content was 38 vol.% but decreased to around 30 vol.%

due to increasing thickness during infiltration [24]. The laminates were impregnated with a phenolic-based slurry containing a powder mixture of elemental B and ZrB_2 before stacking in a 0/90° configuration and curing at 423 K. After pyrolysis, the porous matrix contained B, C and ZrB_2 phases. The porous samples were then infiltrated with B_2O_3 in order to transform the porous carbon from the phenolic into B_4C for infiltration. Material *RMI-1* was infiltrated with liquid Zr 706 (2173 K) whilst material *RMI-2* with Zr_2Cu-1% B was infiltrated at 1473 K.

Table 1. Green preparation method, consolidation techniques, type of fibre preform, compositions expressed as volumetric amount of the ceramic phases and porosity measured by image analysis, and measured geometrical density (ρ).

Sample	Green preparation	Consolidation technique	Fibre preform	Composition	P	ρ
				vol.%	vol.%	g/cm^3
CFHP	Fibre mixing	HP	Chopped fibres	$52ZrB_2+3SiC+38C_f$	7	4.3
MFSPS		SPS	Milled fibres	$49ZrB_2+10SiC+40C_f$	1	4.1
SIHP-1	Slurry impregnation	HP	UD fibre sheet	$48ZrB_2+3SiC+47C_f$	2	4.2
SIHP-2				$46ZrB_2+5SiC+48C_f$	1	4.1
CVI-1	Slurry impregnation	RF-CVI	2.5D preform	$28ZrB_2+23C_f+46PyC$	3	3.1
CVI-2				$15ZrB_2+10SiC+5Y_2O_3+23C_f+37PyC$	10	2.7
RMI-1	Slurry impregnation	RMI	UD fibre sheet	$66(Zr+ZrB_2)+24C_f$	10	4.8
RMI-2				$74(Zr_2Cu+ZrB_2)+20C_f$	6	5.4

All the composites were machined to obtain at least 10 specimens for each composition. The microstructures were analysed by FESEM (FE-SEM, Carl Zeiss Sigma NTS Gmbh Öberkochen, Germany) before and after thermal cycles. Oxidation treatments at 2278 K were carried out in an inductively-heated multipurpose furnace facility, called INDUTHERM, available at the German Aerospace Center (DLR, Stuttgart), Fig. 1. Ramping and isothermal dwelling were controlled via a

two-colour pyrometer which directly commands the heating power unit. The hot chamber was completely lined with porous zirconia blankets: batches of up to six samples were carefully mounted on home-made porous zirconia setters, then two cycles of pumping down to about 1 mbar and Ar flushing up to an inner pressure of 0.6 mbar were completed before ramping up the temperature, at 100 K/min, to the target of 2278 K. The porous zirconia setters had the main function of holding the samples and preventing their interaction at these temperatures. During the temperature ramp the atmosphere was Ar at a pressure of 0.2 mbar, once the targeted temperature was reached, a gas inlet was opened and air started flowing at 5 l/min for 2 min (the filling time of the chamber was about 12 s); a couple of holes permitted the air to flow through and then exit from the opposite side of the chamber.

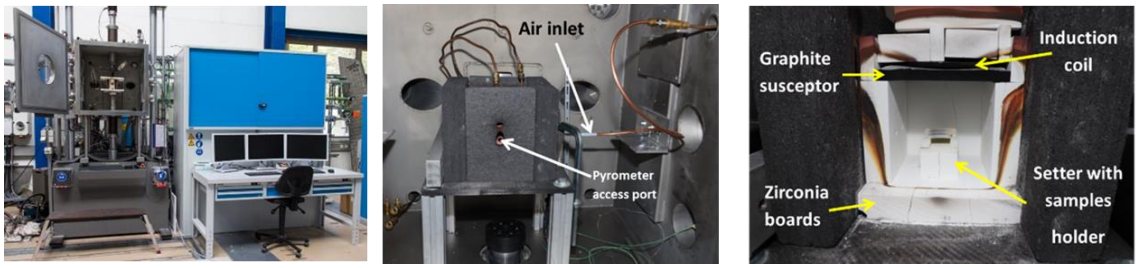

Fig. 1. INDUTHERM: the inductively-heated multipurpose furnace available at the Institute of Structures and Design, German Aerospace Center (Stuttgart, Germany).

Flexural strength (σ) tests in a four-point bending configuration at room temperature were carried out using a fully-articulated steel fixture with a lower span of 20 mm and an upper span of 10 mm; the crosshead speed of a universal testing machine (mod. Z050, ZwickRoell GmbH & Co. KG, Ulm-Einsingen, Germany) was 1 mm min^{-1}. The preferred nominal dimensions of the specimens were 25 × 2.5 × 2.0 mm^3. In the case of the CVI-based compositions, the specimens were machined with a width of 7 mm to ensure that they complied with the 2.5D fibre arrangement. At least three valid tests were performed for each kind of composite.

3 Results and Discussion

3.1 Microstructure of as-produced composites

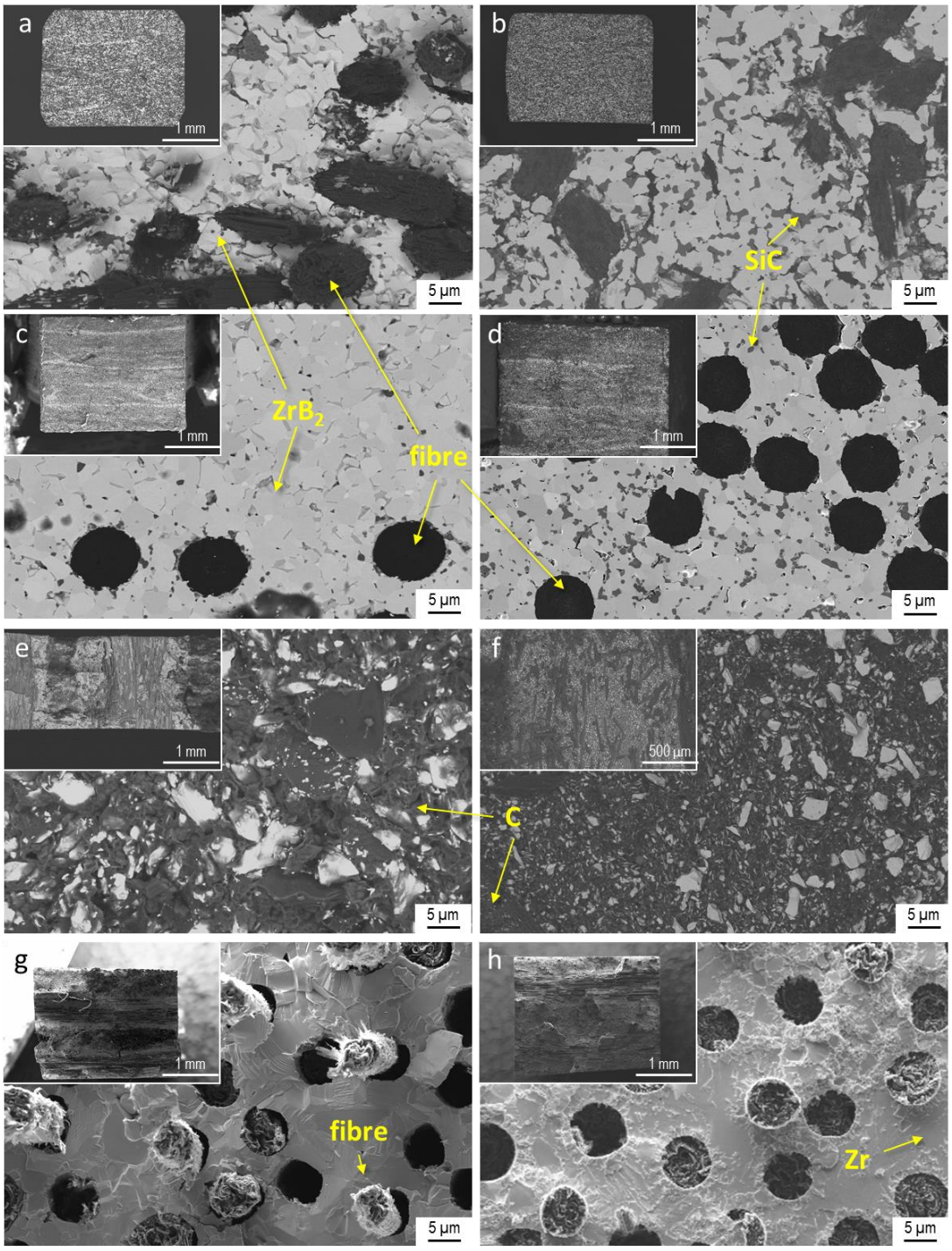

Fig. 2. Microstructure before oxidation of specimens: (a) CFHP and (b) MFSPS showing fibres (black), SiC (dark grey), ZrB_2 (light grey); (c) SIHP-1 and (d) SIHP-2 showing fibres (black), SiC (dark grey), ZrB_2 (light grey); (e) CVI-1 and (f) CVI-2 showing a dark matrix of carbon with white particles of UHTC phases; (g) RMI-1 and (h) RMI-2 showing fibres pull-out from the ceramic/metal matrix.

The different microstructure features are illustrated in Fig. 2 a-h and described below.

- *Sintered short fibre-reinforced ZrB_2/SiC composites (CFHP, MFSPS).* Both specimens displayed a fully dense microstructure with a similar random distribution of fibres, Fig. 2 a,b and insets, that were about 300 µm long for CFHP and 100 µm long for MFSPS. The SiC was homogeneously dispersed in the ZrB_2 matrix and the fibres were well anchored to the matrix. The fracture surface was rather smooth, indicating a strong adhesion with the matrix and limited fibre pull-out, Fig. 2 a. Both specimens contained 40 vol.% fibres, but sample MFSPS had a higher amount of SiC, as evident in Fig. 2 b.

- *Sintered continuous fibre-reinforced ZrB_2/SiC composites (SIHP-1 and 2).* This group of materials comprised two ZrB_2/SiC composites with different SiC contents (5 and 10 vol.% respectively for SIHP-1 and SIHP-2). For both composites, the fibre volumetric content was overall higher than short fibre-reinforced composites (48 vs 40%), whilst a comparable full matrix densification was obtained for both specimens (Fig. 2 c,d insets). Fibres (black) and SiC (dark grey) were homogeneously distributed in the ZrB_2 matrix (light grey) and the fibre/matrix interface was very strong, as can be seen from the intimate contact between the fibres and the surrounding ceramic matrix (Fig. 2 c,d).

- *2.5D fibre-reinforced C/C-ZrB_2 composites fabricated via CVI (CVI-1 and 2).* The third class of materials was constituted by 2.5D fibre-reinforced C/C composites doped with 20-30% ZrB_2 and produced via radio-frequency assisted chemical vapour infiltration. The microstructure of both specimens before testing is shown in Fig. 2 e,f. The complex 2.5D preform architecture is outlined in the insets of Fig. 2 e, f. The C_f/C matrix is represented by the dark regions, while the white spots are ZrB_2 particles. The latter is more easily recognizable in Fig. 2 e as coarse white particles. For specimen CVI-2, the finer particle component was Y_2O_3 (Fig. 2 f). Large pores were more evident in CVI-1 as black isolated spots in Fig. 2e, whilst sample CVI-2 specimens were characterized by a more dense carbon matrix. The lower density of the composite could be attributed to the presence of lighter phases such as SiC and Y_2O_3.

- *Continuous fibre-reinforced Zr/ZrB_2 composites fabricated via RMI (RMI-1 and 2).* These composites were produced by reactive melt infiltration with slightly different procedures, as previously described. For specimen RMI-1, the molten Zr reacted with the boron source (provided by B_4C) to produce in-situ ZrB_2 and ZrC, Fig. 2 g,h. Due to the similar contrast displayed by the constituent phases, a precise quantification of ZrB_2, residual Zr and ZrC was not possible. The final fibre content amounted to ~25%, which was attributed to the swelling of the material during infiltration as previously observed by Vinci et al [24]. For specimen RMI-2, the Zr_2Cu reacted with B_4C, resulting in the formation of ZrB_2/ZrC phases, whilst the majority of residual copper segregated to the surface of the sample. In spite of the lower processing temperature, this sample displayed a higher degree of fibre degradation, suggesting that the Zr_2Cu melt was much more reactive. Because of this, the final fibre content was even lower than RMI-1, amounting to ~20 vol.%. Both specimens were characterized by little or no fibre pull-out. As in the previous work [24], the shrinkage of the metallic phase during cooling led to the fibre/matrix debonding, i.e. a weak interface was formed. In fact, looking at fracture surfaces showed in Fig. 2, it was observed that matrix around fibres was actually detached from the fibre and the perception is that fibre failures close to the crack plane occurred in the crack tip rather than in the crack wake.

3.2 Microstructure after thermal treatment

Thermal treatment at 2278K / 2 min in air led to strong oxidation phenomena. In the absence of any environmental coating, the exposed surfaces underwent C_f and carbon phase burnout that left large pores and oxidation of the matrix phases (ZrB_2, SiC), whilst any metallic phases melted. Features of the oxidised samples are illustrated in Fig. 3 (a-h).

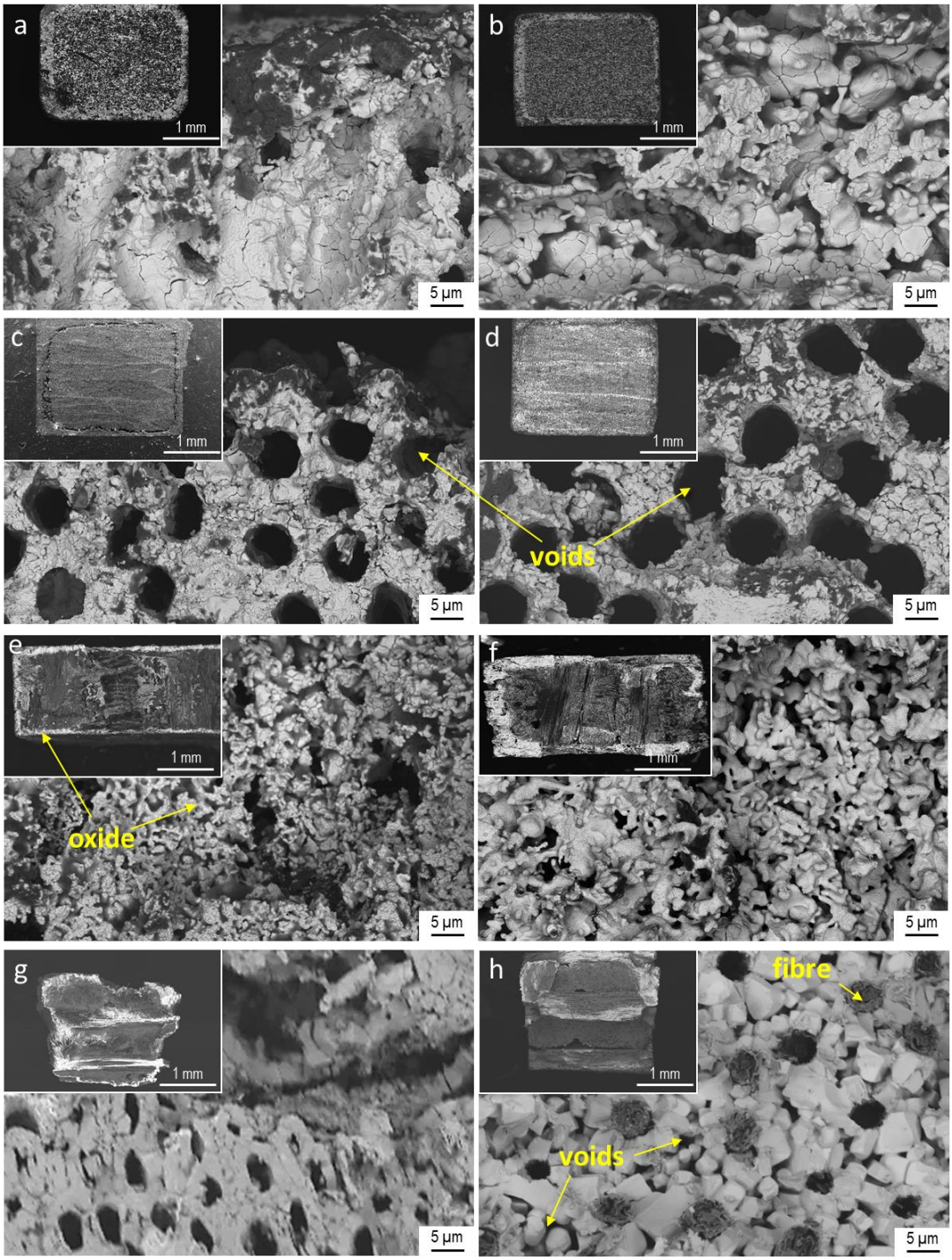

Fig. 3. Microstructure of specimens after oxidation: (a) CFHP and (b) MFSPS: morphology of the ZrO_2 scale; (c) SIHP-1 and (d) SIHP-2: morphology of the ZrO_2 scale and the hollows left by the fibre oxidation; (e) CVI-1 and (f) CVI-2: morphology of the oxidised layer, showing larger ZrO_2 grains for CVI-2, (g) RMI-1 and (h) RMI-2 showing the inhomogeneous oxidation which affected even the bulk material, with the partial loss of the metallic phase.

- *Sintered short fibre-reinforced ZrB_2/SiC composites (CFHP, MFSPS).* After heat treatment at 2278 K in severely oxidizing conditions, CFHP and MFSPS were characterized by the homogeneous oxidation of the outer layer that was mainly characterized by an outer ZrO_2 scale and an inner ZrO_2/SiO_2 layer, Fig. 3 a, b insets. Oxidation of the carbon fibres in the outer layers left holes in the zirconia scale that were only partially filled with silica. The thickness of the oxide layer observed in CFHP, ~170 µm, was slightly higher than for MFSPS, ~140 µm, and this was attributed to the slightly different porosity and SiC content. In both cases the porous nature of the oxide scale produced a brittle layer, Fig. 3 a,b.

- *Sintered continuous fibre ZrB_2/SiC composites (SIHP-1, 2).* Just as observed for the short fibre-reinforced UHTCs, samples SIHP-1 and SIHP-2 were also characterized by the homogeneous oxidation of the outer layer, insets in Fig. 3 c, d, with the formation of an outer ZrO_2 layer and an intermediate porous layer of ZrO_2 and some traces of SiO_2 and the hollows left by the fibre removal, Fig. 3 c, d. Specimen SIHP-1 was characterized by a weaker oxide scale, as evidenced by its tendency to detach from the bulk material, Fig. 3 c. This was attributed to the lower amount of SiC that, during oxidation, provides a source of liquid phase that holds the ZrO_2 grains together. The thickness of the oxide layers was ~100 µm and ~80 µm for SIHP-1 and SIHP-2 respectively, which was lower than for the short fibre-reinforced composites. However, since the oxide layer was quite brittle and prone to detachment from the bulk surface unlike short fibre-reinforced composites, it is believed that the oxidised cross section did not contribute to the mechanical resistance during testing.

- *2.5D fibre-reinforced C/C-ZrB_2 composites fabricated via CVI (CVI-1, 2).* The microstructure of specimens CVI-1 and CVI-2 after heat treatment is shown in Fig. 3, e,f. Both specimens were characterized by the formation of an outer layer of porous ZrO_2, which in the case of CVI-2 displayed a particular morphology due to the presence of Y_2O_3, Fig. 3 f. Specimen CVI-2 had a consistently thicker oxide scale, ~200 µm, Fig. 3 f-inset, compared to CVI-1, ~120 µm, which could be attributed both to the overall lower content of the UHTC and to the layer configuration.

Another reason could be attributed to the partial loss of material during machining which might have created further paths for oxygen diffusion.

- *Continuous fibre-reinforced Zr/ZrB_2 composites fabricated via RMI.* The samples produced by RMI were the most affected by the heat treatment. Beside the carbon fibre burnout, the presence of residual unreacted metals with melting point lower than the heat treatment temperature led to the matrix collapse. Both specimens were characterized by a high degree of oxidation that reached even the interior of the material, Fig. 3 g, h insets. RMI-1 was characterized by the hollows left by the fibre oxidation and by the formation of an inhomogeneous layer of ZrO_2 surrounded by the leftover alloy, Fig. 3 g. In the case of RMI-2, even the internal microstructure was affected, with the loss of the leftover Cu-based alloy that at 2278 K was rapidly removed, leaving a highly porous internal microstructure made up almost entirely of ZrC and residual Zr, Fig. 3 h.

3.3 Flexural strength

The values of flexural strength and stress-displacement curve of as-produced samples are reported in Fig. 4 and Fig. 5, respectively. For the sake of comparison, these figures also show the situation after oxidation at 2278 K. The right-hand ordinate of Fig. 4 a shows the specific strength of as produced composites.

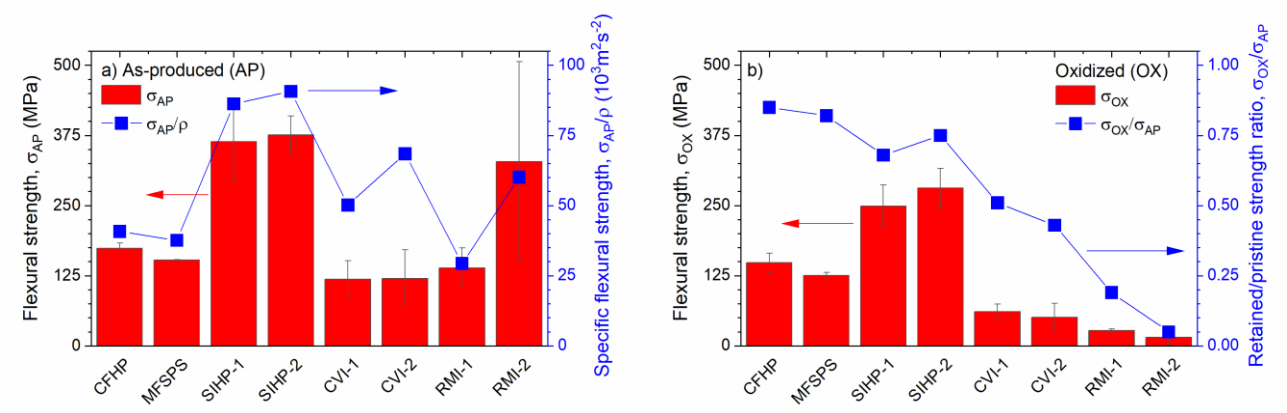

Fig. 4. a) Flexural strength (bars) of as-produced composites. The right-hand ordinate refers to the specific flexural strength (filled symbols). b) Flexural strength (bars) of composites after oxidation. The right-hand ordinate refers to the retained/pristine strength ratio (filled symbols).

- *Pristine flexural strength.* As expected, there is plenty of difference in the mechanical responses among the UHTCMCs, due to the different composites, type of fibre and fibre arrangements. The highest values, 350 MPa, were obtained for composites with no porosity and unidirectional fibres, SIHP-1, SIHP-2 and for the RMI samples. Strength of 150-170 MPa were found for the random chopped fibre-reinforced composites and 120-150 MPa for CVI samples, which had a 2.5D fibre preform arrangement. The degree of scatter around the mean values is also indicative of the different microstructural features. The random short fibre-reinforced samples were very homogenous, whilst increasing the complexity of the arrangement also increased the variability in the strength values. The load displacement curves of the as-produced materials also revealed other interesting features. The short fibre-reinforced composites, Fig. 5 a and b, as well as the continuous fibre-reinforced composites produced by RMI, Fig. 5 g and h, showed a predominantly brittle failure. In the short-fibre composites, this was due to the reduced fibre dimensions (100-300 μm) and dense matrix. In the RMI composites, the matrix-dominated behaviour was ascribed to the dense matrix and to the relatively low fibre volume content, <30 vol.%. The reaction of the molten alloy with the uncoated fibres also jeopardized the flexural strength, which displayed a large data scatter, Fig.4 a. On the other hand, the SIHP and CVI samples displayed damage tolerant behaviour, with flexural test curves similar to other CMCs, Fig. 5 c-f, thanks to the high fibre content and weak matrix / fibre interface, respectively.

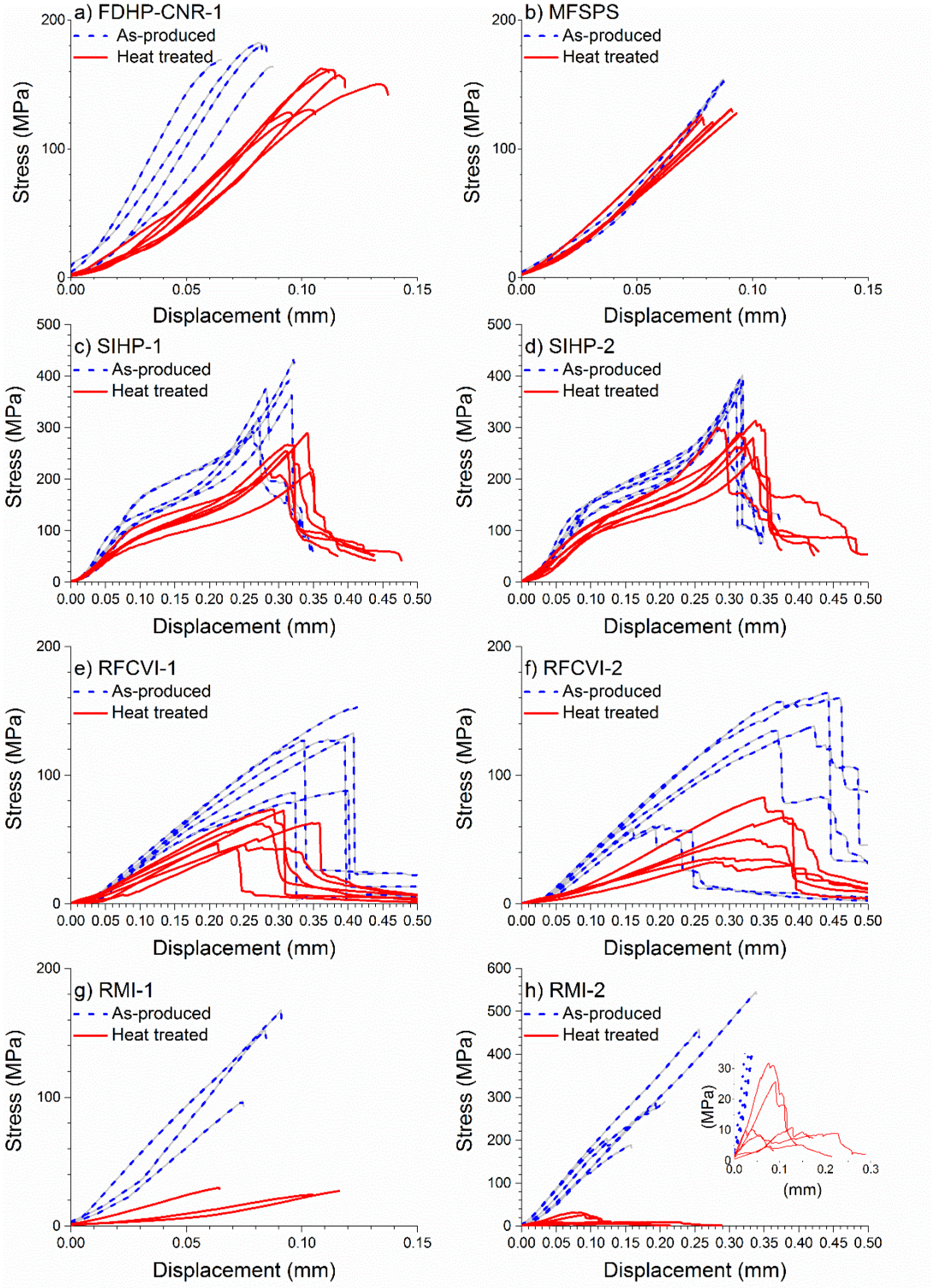

Fig. 5. Stress-displacement curves of as-produced (dotted curves) and heat treated at 2278 K (solid curves) specimens: a) chopped fibre dispersion and hot-pressing sintered UHTC (CFHP); b) milled short fibre dispersion and spark plasma sintered UHTC (MFSPS); c, d) 0/0° continuous carbon fibre-reinforced UHTC by slurry infiltration and sintering by hot-pressing (SIHP); e,f) 2.5D ultra-high temperature ceramic matrix composites by chemical vapor infiltration (CVI-1) and RF heated chemical vapour infiltration (CVI-2); g,h)

0/90° continuous carbon fibre-reinforced UHTC by reactive melt infiltration (RMI). h-inset) zoom of the curves of the heat treated RMI-2 samples.

- *Retained flexural strength after heat treatment at 2278 K.* Values and curves of strength after sample oxidation are reported in Fig. 4 b and 5. The right-hand ordinate of Fig. 4 b shows the retained / initial strength ratio. In all cases, the failure mode, brittle or non-brittle, did not change within each class of composite, see Fig. 5. On the contrary, the slope of the curves showed a notable variation, indicating a marked change in the modulus. The loss of strength was related to the effects of oxidation at 2278 K inducing a significant level of damage at the surface. Assuming that for most of the samples the bulk damage was less important, the formation of a compact and dense oxide resulted in minimum variation of the strength. On the contrary, a highly damaged external layer severely impacted the strength.

Fig. 5 shows that both types of short fibre-reinforced composites, CFHP and MFSPS, maintained the highest values of retained strength, above 80% of the initial values. This was attributed to the higher amount of protective ceramic matrix (60 vol.%) surrounding the carbon fibres and the very low amount of residual porosity, which was <1 vol.%. Since the internal microstructure was unchanged, the resulting decrease in strength can be simply attributed to the smaller cross section under loading and the lower strength contribution provided by the oxide scale. In the case of the MFSPS, the limited oxidized layer allowed the stiffness to be retained, as demonstrated by the overlapping nature of the curves of the as-produced and thermally treated specimens, Fig. 5 b.

For sintered composites with continuous fibres, SIHP-1 and 2, their retained strength decreased to around 70% of the unoxidised values. In this case, the higher amount of carbon fibres, 47-48%, left large empty channels in the scale, increasing the rate of oxidation and making the scale more brittle.

The CVI samples retained 40-50 % of their original strength, which was attributed to the original residual porosity, higher than 10%, and the high amount of carbon phase originally present, both in the form of fibre and pyrolytic carbon, both of which will have burnt out leading to an increase in

the oxidation kinetics. Finally, the RMI composites showed the lowest retained strength, below 20%. This result was expected because the heat treatment at 2278 K strongly damaged the matrix down to the centre of the cross section, leaving a discontinuous microstructure.

4 Conclusions

For the first time, the flexural strength of different types of UHTCMCs has been compared before and after oxidation at 2278 K in air. All the composites were damaged to some extent by the oxidation of the most vulnerable phase, the C, which led to the formation of pores and channels and hampered the formation of a fully protective oxide scale. The short fibre-reinforced composites showed the best oxidation resistance and a retained strength higher than 80% of its original value thanks to the dense matrix and the limited amount of fibres present (40 vol.%). The continuous fibre-reinforced composites, which were characterized by 50 vol.% of fibre and a dense UHTC matrix, maintained ~70% of their original strength. With an increase in the amount of carbon phase present, the RF-CVI-based samples, the retained strength decreased down to ~50%. Nevertheless, all UHTCMCs with a ZrB_2-based ceramic matrix demonstrated the ability to sustain extreme temperatures in an air environment with a promising degree of strength retention. In contrast, the UHTCMCs processed by the RMI technique were found to be unsuitable for application at such a high temperature, due to the presence of unreacted residual metal that led to a severe loss of matrix stability.

Acknowledgements

This work has received funding from the European Union's Horizon 2020 "Research and innovation programme" under grant agreement No 685594 (C^3HARME). The authors of CNR-ISTEC greatly acknowledge AM^3aC^2A project (ASI N. 2020-4-U.0).

References

[1] Sciti D, Silvestroni L, Monteverde F, Vinci A, Zoli L. Introduction to H2020 project C^3HARME–next generation ceramic composites for combustion harsh environment and space. Advances in Applied Ceramics 2018. doi:10.1080/17436753.2018.1509822.

[2] Zoli L, Sciti D, Vinci A, Galizia P, Monteverde F, Failla S, et al. Ultra-High Temperature Ceramic Matrix Composites. Reference Module in Materials Science and Materials Engineering, Elsevier; 2020. doi:10.1016/B978-0-12-818542-1.00023-0.

[3] Zhang D, Hu P, Dong S, Liu X, Wang C, Zhang Z, et al. Oxidation behavior and ablation mechanism of C_f/ZrB_2-SiC composite fabricated by vibration-assisted slurry impregnation combined with low-temperature hot pressing. Corrosion Science 2019;161:108181. doi:10.1016/j.corsci.2019.108181.

[4] Ouyang H, Zhang Y, Li C, Li G, Huang J, Li H. Effects of ZrC/SiC ratios on mechanical and ablation behavior of C/C–ZrC–SiC composites prepared by carbothermal reaction of hydrothermal co-deposited oxides. Corrosion Science 2019;163:108239. doi:10.1016/j.corsci.2019.108239.

[5] Rueschhoff LM, Carney CM, Apostolov ZD, Cinibulk MK. Processing of fiber-reinforced ultra-high temperature ceramic composites: A review. International Journal of Ceramic Engineering & Science 2020;2:22–37. doi:10.1002/ces2.10033.

[6] Chen BW, Ni DW, Liao CJ, Jiang YL, Lu J, Dong SM. Long-term ablation behaviour and mechanisms of 2D-C_f/ZrB_2-SiC composites at temperatures up to 2400 °C. Corrosion Science 2020;177:108967. doi:10.1016/j.corsci.2020.108967.

[7] Chen X, Feng Q, Zhou H, Dong S, Wang J, Cao Y, et al. Ablation behavior of three-dimensional C_f/SiC-ZrC-ZrB_2 composites prepared by a joint process of sol-gel and reactive melt infiltration. Corrosion Science 2018;134:49–56. doi:10.1016/j.corsci.2018.02.011.

[8] Huang D, Zhang M, Huang Q, Wang L, Xue L, Tang X, et al. Ablation mechanism of C/C-ZrB_2-ZrC-SiC composite fabricated by polymer infiltration and pyrolysis with preform of C_f/ZrB_2. Corrosion Science 2015;98:551–9. doi:10.1016/j.corsci.2015.05.064.

[9] Zhuang L, Fu QG, Liu TY. Ablation resistance of wedge-shaped C/C-ZrB_2-ZrC-SiC composites

exposed to an oxyacetylene torch. Corrosion Science 2016;112:462–70. doi:10.1016/j.corsci.2016.08.010.

[10] Hu C, Pang S, Tang S, Wang S, Huang H, Cheng HM. Ablation and mechanical behavior of a sandwich-structured composite with an inner layer of C_f/SiC between two outer layers of C_f/SiC-ZrB_2-ZrC. Corrosion Science 2014;80:154–63. doi:10.1016/j.corsci.2013.11.019.

[11] Tang S, Deng J, Wang S, Liu W. Comparison of thermal and ablation behaviors of C/SiC composites and C/ZrB_2-SiC composites. Corrosion Science 2009;51:54–61. doi:10.1016/j.corsci.2008.09.037.

[12] Hald H. Operational limits for reusable space transportation systems due to physical boundaries of C/SiC materials. Aerospace Science and Technology 2003;7:551–9. doi:10.1016/S1270-9638(03)00054-3.

[13] Wang X, Wei K, Tao Y, Yang X, Zhou H, He R, et al. Thermal protection system integrating graded insulation materials and multilayer ceramic matrix composite cellular sandwich panels. Composite Structures 2019;209:523–34. doi:10.1016/J.COMPSTRUCT.2018.11.004.

[14] Binner J, Porter M, Baker B, Zou J, Venkatachalam V, Diaz VR, et al. Selection, processing, properties and applications of ultra-high temperature ceramic matrix composites, UHTCMCs – a review. International Materials Reviews 2019:1–56. doi:10.1080/09506608.2019.1652006.

[15] Zhang D, Feng J, Hu P, Xun L, Liu M, Dong S, et al. Enhanced mechanical properties and thermal shock resistance of C_f/ZrB_2-SiC composite via an efficient slurry injection combined with vibration-assisted vacuum infiltration. Journal of the European Ceramic Society 2020. doi:10.1016/j.jeurceramsoc.2020.07.003.

[16] Hu P, Cheng Y, Zhang D, Xun L, Liu M, Zhang C, et al. From ferroconcrete to C_f/UHTC-SiC: A totally novel densification method and mechanism at 1300 °C without pressure. Composites Part B: Engineering 2019;174:107023. doi:10.1016/j.compositesb.2019.107023.

[17] Liu Y, Zu Y, Tian H, Dai J, Sha J. Microstructure and mechanical properties of continuous carbon fiber-reinforced ZrB_2-based composites via combined electrophoretic deposition and

sintering. Journal of the European Ceramic Society 2020. doi:10.1016/j.jeurceramsoc.2020.10.044.
[18] Vinci A, Zoli L, Sciti D, Watts J, Hilmas GE, Fahrenholtz WG. Mechanical behaviour of carbon fibre reinforced TaC/SiC and ZrC/SiC composites up to 2100°C. Journal of the European Ceramic Society 2019;39:780–7. doi:10.1016/j.jeurceramsoc.2018.11.017.
[19] Galizia P, Zoli L, Sciti D. Impact of residual stress on thermal damage accumulation, and Young's modulus of fiber-reinforced ultra-high temperature ceramics. Materials & Design 2018;160:803–9. doi:10.1016/J.MATDES.2018.10.019.
[20] Galizia P, Sciti D, Saraga F, Zoli L. Off-axis damage tolerance of fiber-reinforced composites for aerospace systems. Journal of the European Ceramic Society 2020;40:2691–8. doi:10.1016/j.jeurceramsoc.2019.12.038.
[21] Cheng T. Understanding the ultra-high-temperature mechanical behaviors of advanced two-dimensional carbon-carbon composites. Ceramics International 2020. doi:10.1016/j.ceramint.2020.05.237.
[22] Li L. Modeling temperature-dependent vibration damping in C/SiC fiber-reinforced ceramic-matrix composites. Materials 2020;13:1633. doi:10.3390/ma13071633.
[23] Baker B, Rubio V, Ramanujam P, Binner J, Hussain A, Ackerman T, et al. Development of a slurry injection technique for continuous fibre ultra-high temperature ceramic matrix composites. Journal of the European Ceramic Society 2019;39:3927–37. doi:10.1016/j.jeurceramsoc.2019.05.070.
[24] Vinci A, Zoli L, Galizia P, Kütemeyer M, Koch D, Sciti D. Reactive melt in\filtration of carbon fibre reinforced ZrB_2/B composites with Zr_2Cu. Composites Part A: Applied Science and Manufacturing 2020:105973. doi:10.1016/j.compositesa.2020.105973.

Figure captions

Fig. 1. INDUTHERM: the inductively-heated multipurpose furnace available at the Institute of Structures and Design, German Aerospace Center (Stuttgart, Germany).

Fig. 2. Microstructure before oxidation of specimens: (a) CFHP and (b) MFSPS showing fibres (black), SiC (dark grey), ZrB_2 (light grey); (c) SIHP-1 and (d) SIHP-2 showing fibres (black), SiC (dark grey), ZrB_2 (light grey); (e) CVI-1 and (f) CVI-2 showing a dark matrix of carbon with white particles of UHTC phases; (g) RMI-1 and (h) RMI-2 showing fibres pull-out from the ceramic/metal matrix.

Fig. 3. Microstructure of specimens after oxidation: (a) CFHP and (b) MFSPS showing the morphology of the ZrO_2 scale; (c) SIHP-1 and (d) SIHP-2 showing the morphology of the ZrO_2 scale and the hollows left by the fibre oxidation; (e) RMI-1 and (f) RMI-2 showing the inhomogeneous oxidation which affected even the bulk material, with the partial loss of the metallic phase.

Fig. 4. a) Flexural strength (bars) of as-produced composites. The right-hand ordinate refers to the specific flexural strength (filled symbols). b) Flexural strength (bars) of composites after oxidation. The right-hand ordinate refers to the retained/pristine strength ratio (filled symbols).

Fig. 5. Stress-displacement curves of as-produced (dotted curves) and heat treated at 2278 K (solid curves) specimens: a) chopped fibre dispersion and hot-pressing sintered UHTC (CFHP); b) milled short fibre dispersion and spark plasma sintered UHTC (MFSPS); c, d) 0/0° continuous carbon fibre-reinforced UHTC by slurry infiltration and sintering by hot-pressing (SIHP); e,f) 2.5D ultra-high temperature ceramic matrix composites by chemical vapor infiltration (CVI-1) and radio frequency assisted chemical vapor infiltration (CVI-2); g,h) 0/90° continuous carbon fibre-reinforced UHTC by reactive melt infiltration (RMI). h-inset) zoom of the curves of the heat treated RMI-2 samples.